

# Microturbulence in DIII-D tokamak pedestal. IV. Electrostatic turbulent transport

X. Liao,<sup>1</sup> Z. Lin,<sup>2</sup> I. Holod,<sup>2</sup> B. Li,<sup>1,a)</sup> and G. Y. Sun<sup>3</sup>

<sup>1</sup>Fusion Simulation Center, State Key Laboratory of Nuclear Physics and Technology, School of Physics, Peking University, Beijing 100871, China

<sup>2</sup>Department of Physics and Astronomy, University of California, Irvine, California 92697, USA

<sup>3</sup>Department of Physics, and Institute of Theoretical Physics and Astrophysics, Xiamen University, Xiamen 361005, China

(Received 20 June 2016; accepted 25 November 2016; published online 16 December 2016)

Gyrokinetic simulations of electrostatic microturbulence in the edge plasmas of DIII-D shot 131997 find that the geodesic acoustic mode (GAM) is generated after nonlinear saturation both at the pedestal top and in the peak gradient region, and in turn, regulates the turbulence in both regions. Collisions significantly reduce the GAM amplitude and the associated GAM modulation of the turbulence in both regions. Collisions have little effects on the ion temperature gradient turbulent transport level at the pedestal top. On the other hand, collisional damping of the TEM significantly reduces the turbulent transport level in the peak gradient region. *Published by AIP Publishing.* [<http://dx.doi.org/10.1063/1.4972080>]

## I. INTRODUCTION

Anomalous cross-field particle, energy and momentum transport in tokamak plasmas is generally believed due to microturbulence excited by drift wave instabilities.<sup>1</sup> The turbulent transport mechanism for ions and electrons in core plasmas is relatively clear thanks to intensive studies of turbulence in experiment, theory, and simulation in the past decades.<sup>2,3</sup> Recently, more attention has been shifted to the studies of turbulence and transport in the tokamak edge, since they are more complicated and crucial for the high confinement mode (H-mode).<sup>4</sup> The H-mode operation is characterized by steep gradients of density and temperature in the edge region, which can provide a source of free energy to drive a number of instabilities, such as electrostatic ion/electron temperature gradient driven modes (ITG/ETG),<sup>5,6</sup> trapped electron mode (TEM),<sup>7-9</sup> and electromagnetic kinetic ballooning mode (KBM).<sup>10-12</sup> The ITG, TEM, and KBM are long wavelength instabilities with  $k_{\theta}\rho_i < 1$  and ETG is short wavelength instability with  $k_{\theta}\rho_i \gg 1$ , where  $k_{\theta}$  is the poloidal wavenumber and  $\rho_i$  is the ion gyroradius.

A number of experiments and simulations have found that zonal flows,<sup>2,13</sup> which are self-generated by the turbulence, play a very important role in modulating and setting the level of turbulence and transport because of their shearing effects on turbulence. There are two types of zonal flows: one is the low frequency zonal flow (LFZF), mainly seen in the core plasmas; and the other is the higher frequency geodesic acoustic mode (GAM),<sup>14</sup> usually seen in the edge plasmas with a higher safety factor. We know better the characteristics of LFZF and its effects on turbulence in the core plasmas.<sup>2</sup> However, the role of the GAM in

turbulence and transport in the edge plasmas especially in the pedestal region is less well understood. Moreover, collisions can play important roles in the edge turbulence and transport.

In this work, we use the gyrokinetic toroidal code (GTC)<sup>2,15,16</sup> to study the electrostatic turbulence, the generation of GAM, and its effects on turbulence and transport in a DIII-D (shot 131997) H-mode pedestal plasma.<sup>5,8,12</sup> Collisions are included in our simulations using the Lorentz pitch angle scattering operator for electron-ion collisions and the Fokker-Planck operator for electron-electron and ion-ion collisions.<sup>17</sup> Our simulations find that GAM is generated after nonlinear saturation both at the pedestal top and in the peak gradient region, and in turn, regulates the turbulence in both regions. Collisions significantly reduce the GAM amplitude and the associated GAM modulation of the turbulence in both regions. In the pedestal top with a relatively high temperature, collisions have little effects on the ITG turbulent transport level. In the peak gradient region, collisional damping of the TEM significantly reduces the turbulent transport level. We emphasize that the current simulations do not cover the separatrix and scrape-off layer (SOL) and do not include the mechanism sustaining the tokamak H-mode.

The remainder of this paper is organized as follows: Section II describes the simulation model. The nonlinear simulation results are presented for the pedestal top and the peak gradient region in Sec. III. Finally, conclusions are given in Sec. IV.

## II. SIMULATION MODEL

In GTC particle-in-cell simulations, the plasma is treated as a set of marker particles interacting with each other through self-generated electromagnetic fields. The electrostatic version of gyrokinetic equations describing toroidal plasmas in GTC is formulated as follows:<sup>18</sup>

<sup>a)</sup>Author to whom correspondence should be addressed. Electronic mail: bli@pku.edu.cn

$$\left[ \frac{\partial}{\partial t} + \dot{\mathbf{X}} \cdot \nabla + \dot{v}_{\parallel} \frac{\partial}{\partial v_{\parallel}} \right] f_{\alpha} = C_{\alpha}(f_{\alpha}), \quad (1)$$

$$\dot{\mathbf{X}} = v_{\parallel} \frac{\mathbf{B}}{B_0} + \mathbf{V}_E + \mathbf{V}_c + \mathbf{V}_g, \quad (2)$$

$$\dot{v}_{\parallel} = -\frac{1}{m_{\alpha} B_0} \cdot (\mu \nabla B_0 + Z_{\alpha} \nabla \phi). \quad (3)$$

Here,  $f_{\alpha}$  is the distribution function in terms of gyrocenter position  $\mathbf{X}$ , magnetic moment  $\mu$ , and parallel velocity  $v_{\parallel}$ .  $Z_{\alpha}$  is the particle charge,  $m_{\alpha}$  is the particle mass of a species  $\alpha$ , and  $C_{\alpha}$  is the collision operator, with the pitch angle scattering operator for electron-ion collisions<sup>17</sup>  $C_{ei}(\delta f_e) = \nu_{ei} \frac{1}{2} \frac{\partial}{\partial \xi} (1 - \xi^2) \frac{\partial}{\partial \xi} \delta f_e$  and the Fokker-Planck operator for like-species collisions<sup>17</sup>  $C_{\alpha\alpha}(\delta f_{\alpha}) = \frac{\partial}{\partial v_{\parallel}} (\nu_{s\parallel} \delta f_{\alpha}) + \frac{\partial}{\partial v_{\perp}^2} (\nu_{s\perp} \delta f_{\alpha}) + \frac{\partial^2}{\partial v_{\parallel} \partial v_{\perp}^2} (\nu_{\parallel\perp} \delta f_{\alpha}) + \frac{1}{2} \frac{\partial^2}{\partial v_{\parallel}^2} (\nu_{\parallel} \delta f_{\alpha}) + \frac{1}{2} \frac{\partial^2}{(\partial v_{\perp}^2)^2} (\nu_{\perp} \delta f_{\alpha}) + P$ . Here,  $\xi$  is the particle pitch with respect to magnetic field line  $\xi = \frac{v_{\parallel}}{v}$ ,  $\nu_{ei}$  is the electron-ion collision frequency,  $\delta f_{\alpha}$  is the perturbed distribution function,  $v_{\perp}$  is the perpendicular velocity, and  $P$  accounts for the momentum and energy conservation. The definitions of all the collision coefficients  $\nu$  can be found in Ref. 17.  $B_0$  is the equilibrium magnetic field,  $\mathbf{B} = \mathbf{B}_0 + \delta\mathbf{B}$ , and

$$\mathbf{B}^* = \mathbf{B}_0^* + \delta\mathbf{B} = \mathbf{B}_0 + \frac{B_0}{v_{\parallel} \Omega_{\alpha}} \nabla \times \mathbf{b}_0 + \delta\mathbf{B},$$

where  $\mathbf{V}_E$ ,  $\mathbf{V}_c$ , and  $\mathbf{V}_g$  are  $\mathbf{E} \times \mathbf{B}$  the drift velocity, magnetic curvature drift velocity, and grad-B drift velocity, respectively.

$$\mathbf{V}_E = \frac{c \mathbf{b}_0 \times \nabla \phi}{B_0},$$

$$\mathbf{V}_c = \frac{v_{\parallel}^2}{\Omega_{\alpha}} \nabla \times \mathbf{b}_0,$$

$$\mathbf{V}_g = \frac{\mu}{m_{\alpha} \Omega_{\alpha}} \mathbf{b}_0 \times \nabla B_0.$$

The electrostatic potential  $\phi$  is given by the gyrokinetic Poisson equation

$$\frac{4\pi Z_i^2 n_i}{T_i} (\phi - \tilde{\phi}) = 4\pi (Z_i n_i - e n_e), \quad (4)$$

where  $\tilde{\phi}$  is the second-gyroaveraged potential,<sup>19</sup> density  $n_{\alpha}$  is the fluid moment of the corresponding distribution function, and  $\Omega_{\alpha}$  is the cyclotron frequency.

To reduce the particle noise, we use the perturbative ( $\delta f$ ) method<sup>20,21</sup> to solve for the perturbed distribution functions in the full DIII-D geometry. For simulations presented in this paper, we use gyrokinetic equations to deal with ion dynamics, which are valid for the present edge ordering  $\frac{V_E}{v_{th}} \approx k_{\perp} \rho_i \frac{q_i \delta \phi}{T} \sim \frac{\omega}{\Omega_i} \sim \frac{\rho_i}{L_p} \sim \frac{L_p}{R} \sim \varepsilon \ll 1.8$ . Here,  $v_{th}$  is the thermal velocity,  $k_{\perp}$  is the wavenumber perpendicular to the equilibrium magnetic field,  $q_i$  is the charge of the main ion species,  $\delta \phi$  is the perturbed electrostatic potential,  $T$  is the temperature,

$\omega$  is the instability frequency,  $L_p$  is the pressure gradient scale length, and  $R$  is the major radius. Drift kinetic equations are used for electron dynamics because of their small gyro-radius. An electrostatic fluid-kinetic hybrid model based on the expansion of the electron response into adiabatic and non-adiabatic parts is employed for electrons instead of the drift kinetic model to avoid numerical constraints introduced by electron drift kinetic equations.<sup>22</sup> The boundary conditions for field quantities are zero at the radial boundary so that all turbulence-driven fluctuations go smoothly to zero at the radial boundaries and periodic in the poloidal and toroidal directions. Particles going out of the radial boundary are put back into the simulation domain but with the negative sign of the poloidal angle with the domain of  $[-\pi, \pi]$ .

The equilibrium profiles are based on DIII-D discharge 131997 at time 3011 ms,<sup>23</sup> which is a pedestal recovery period in the Edge Localized Mode cycle, as seen in Fig. 1. The equilibrium is implemented in GTC by using the same process presented in Ref. 8, that is, the full plasma profiles, density, temperature, and their gradients  $d \ln(n, T) / d \psi_n$  are replaced by constant values taken from local points of interest within the entire simulation domain, where  $\psi_n$  is the poloidal magnetic flux normalized by its value at the separatrix. Full  $q$ -profile and realistic non-circular, up-down asymmetric magnetic geometry are used in the simulations. The metrics entering the Poisson equation is calculated by the distorted DIII-D mesh points while the kinetic equations are still solved in a flux coordinate system. We focus on two radial locations: the top of the pedestal at a normalized magnetic poloidal flux  $\psi_n = 0.95$ , where the electron temperature gradient first begins to rapidly increase, and the peak gradient region of the pedestal (maximum  $dP/d\psi$ , where  $P$  is the total pressure) at

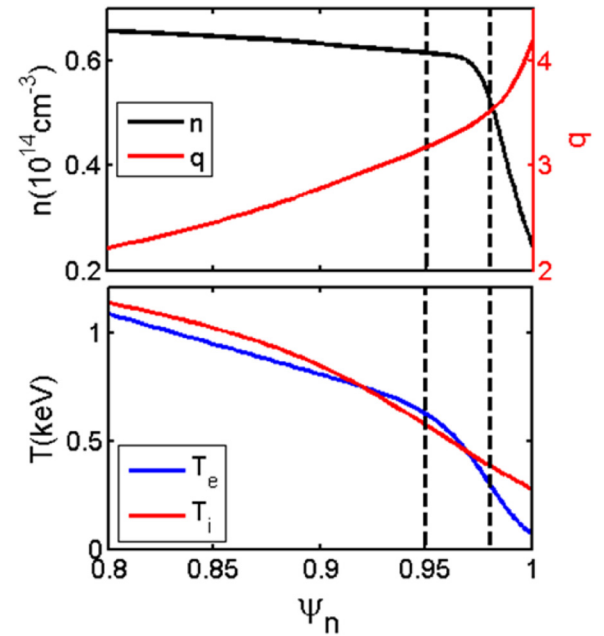


FIG. 1. Plasma profiles in the pedestal region of DIII-D discharge 131997 at time 3011 ms as functions of normalized poloidal flux ( $\psi_n$ ). The upper panel shows density ( $n_i = n_e$ ) and safety factor ( $q$ ) profiles, and the lower panel shows ion and electron temperature ( $T_i$  and  $T_e$ ) profiles. The vertical black dashed lines indicate the radial position of the pedestal top ( $\psi_n = 0.95$ ) and peak gradient region ( $\psi_n = 0.98$ ).

TABLE I. Parameters from DIII-D shot 131997 at  $\psi_n = 0.95$  (pedestal top) and  $\psi_n = 0.98$  (peak gradient region).

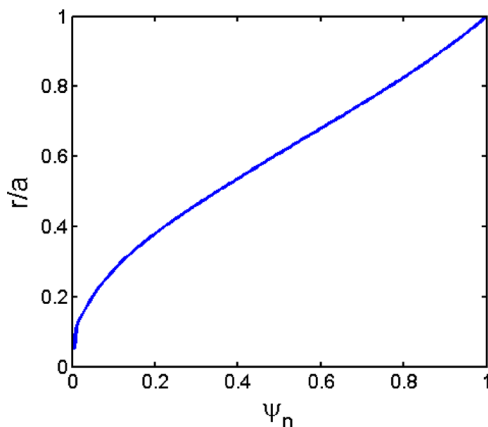
|              | $\psi_n = 0.95$ | $\psi_n = 0.98$ |
|--------------|-----------------|-----------------|
| $T_i/T_e$    | 0.92            | 1.28            |
| $R_0/L_n$    | 2               | 50              |
| $R_0/L_{Te}$ | 25              | 120             |
| $R_0/L_{Ti}$ | 30              | 60              |
| $q$          | 3.17            | 3.53            |
| $\nu_{*i}$   | 0.07            | 0.14            |
| $\nu_{*e}$   | 0.05            | 0.20            |

$\psi_n = 0.98$ , shown as the vertical black dashed lines in Fig. 1. Comparisons of the parameters of these two positions are listed in Table I. Here, the effective collision frequency is defined as  $\nu_{*i} = \varepsilon^{-3/2} \nu_{\alpha} \sqrt{2} q R_0 / v_{th\alpha}$ , and  $v_{th\alpha} = \sqrt{T_{\alpha}/m_{\alpha}}$  is the thermal velocity. The main differences between the two positions are that the density, electron temperature gradients, and collisional frequency are much larger in the peak gradient region than in the pedestal top. For the simulations presented in this paper, a small radial simulation domain size is used, with  $\psi_n = 0.8-1.0$ , which includes the whole pedestal. The density and temperature gradients are set constant within the entire simulation domain by single parameters taken from the two radial positions in Fig. 1. A wider radial domain size should be used in the future to quantitatively compare with experimental measurements since boundary conditions would affect the turbulent transport level. Other parameters are: major radius  $R_0 = 1.76$  m, minor radius defined by the horizontal distance from the axis to the separatrix  $a = 0.72$  m, toroidal magnetic field  $B_0 = 2.03$  T, and deuterium to electron mass ratio  $m_D/m_e = 3672$ . The relationship between minor radius  $r$  and normalized poloidal flux  $\psi_n$  is shown in Fig. 2. Collisions are included in our simulations since collisional effects may be important in edge plasmas with a relative low temperature.

### III. NONLINEAR SIMULATION RESULTS

#### A. Pedestal top

The dominant electrostatic instability in the pedestal top is ITG with a typical ballooning structure in the linear

FIG. 2. The relationship between minor radius  $r$  and normalized poloidal flux  $\psi_n$ .

phase.<sup>12</sup> To verify the validity of nonlinear simulations, noise-driven transport should be small enough so as not to influence the physical transport. The noise-driven heat conductivity can be calculated by using a quasilinear theory, which scales with the square of the particle weight.<sup>24</sup> The noise-driven transport can be reduced by increasing the particle number in the simulations. Time history of volume-averaged heat conductivity and noise-driven heat conductivity for both electrons and ions is shown in Fig. 3 for 200 particles per cell. Here, the heat conductivity is calculated by  $\chi = QL_T/T$ ,  $Q$  is the heat flux measured from simulations,  $Q = \int \frac{1}{2} m v^2 \delta v_r \delta f d^3 v$ , where  $\delta v_r$  is the radial  $\mathbf{E} \times \mathbf{B}$  drift and  $v$  is the velocity. We can see that ITG first grows exponentially and then saturates around time  $t = 17R_0/v_i$ . After the saturation, the noise-driven heat flux is about three-orders of magnitudes smaller than the turbulence-driven heat flux for both ions and electrons. Ions have a higher transport level than electrons, consistent with the fact that the ITG is the most unstable mode in the pedestal top of this DIII-D experiment.

Time evolutions of zonal electric field  $E_r$  ( $m=n=0$ ,  $m$  and  $n$  are poloidal and toroidal mode numbers, respectively) at a fixed radial location are shown in Fig. 4 (blue dotted-dashed curve). The zonal flow is spontaneously generated by the ITG turbulence in the nonlinear stage and oscillates at a constant frequency. We identify this finite frequency mode as the geodesic acoustic mode (GAM). In the edge region with a high  $q$  value, GAM dominates over low frequency zonal flow because of its low damping rate.<sup>25</sup> The frequency of the GAM is given by<sup>25</sup>

$$\omega_{\text{GAM}}^2 = \left( \frac{7}{4} + \tau \right) \frac{2v_i^2}{R^2} \left[ 1 + \frac{46 + 32\tau + 8\tau^2}{(7 + 4\tau)^2 q^2} \right]. \quad (5)$$

By using function  $E_r(t) = A_1 e^{-\gamma t} \cos(\omega_{\text{GAM}} t + \alpha)$  to fit the curve, the GAM frequency calculated from the simulation is about  $2.71 v_i/R_0$ , roughly 39.3 kHz, which is close to  $2.47 v_i/R_0$  from the analytic calculation using Equation (5). Here,  $A_1$  is the amplitude of  $E_r$ ,  $\omega_{\text{GAM}}$ , and  $\gamma$  are the GAM real frequency and damping rate, and  $\alpha$  is the initial phase.

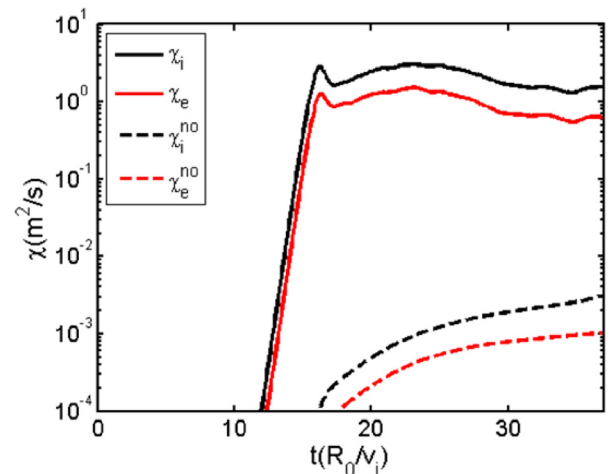


FIG. 3. Time history of volume-averaged total heat conductivity (solid line) and noise-driven heat conductivity (dashed line) for both electrons and ions.

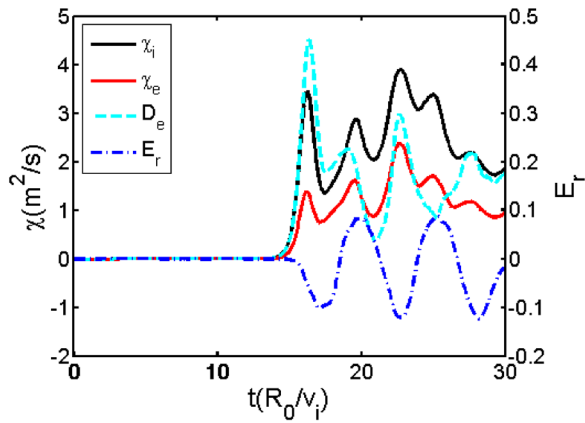


FIG. 4. Time evolutions of the GAM electric field at the flux surface of  $r = 0.87a$ , volume-averaged heat conductivities for ions and electrons, and particle diffusivity from the collisionless simulation of the pedestal top.

Time evolutions of volume-averaged heat conductivities for electrons and ions and particle diffusivity are also shown in Fig. 4. Here, particle diffusivity is defined by  $D = \Gamma L_n / n_0$ ,  $\Gamma$  is the particle flux measured from simulations,  $\Gamma = \int \delta v_r \delta f d^3 v$ . We can see that turbulence grows first and drives the GAM, which has a time delay from the turbulence. The GAM amplitude grows up while the turbulence intensity decays due to GAM, and then turbulence grows again while the GAM decays. Both positive and negative peaks of the GAM correspond to a reduction of heat conductivities, so the heat conductivities oscillate at approximately twice that of the GAM frequency.

The time-radial structure of the GAM electric field  $E_r$  is shown in Fig. 5. The upper panel is with no collisions and lower panel with collisions. The GAM oscillation is very clear. By comparing GAM amplitudes between collisionless and collisional cases, we can see the collisional damping of the GAM. Ion-ion collisions contribute to most of the GAM damping<sup>26</sup> as the Landau damping by ions<sup>27</sup> and trapped electrons<sup>28</sup> is small

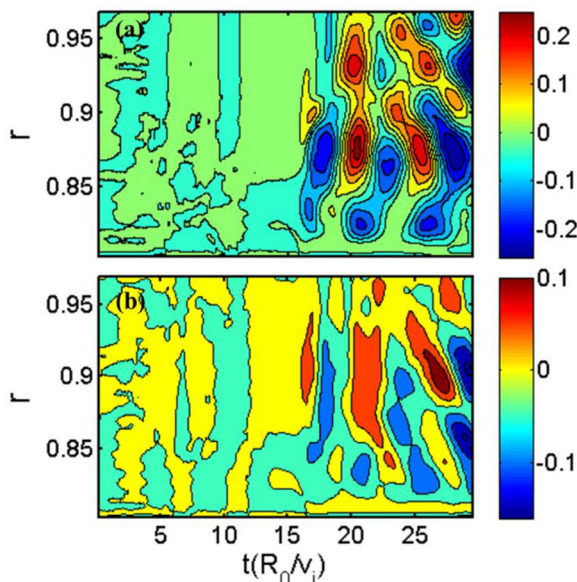


FIG. 5. GAM electric field  $E_r$  structure as a function of time and radial position at the pedestal top for (a) no collisions and (b) with collisions.

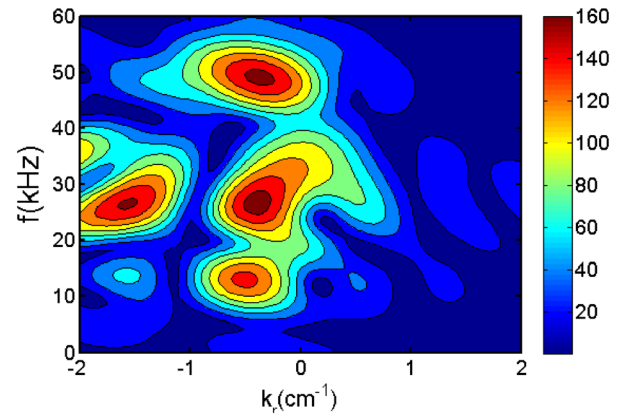


FIG. 6. The radial wavenumber-frequency spectrum  $E(k_r, f)$  of the GAM at the pedestal top without collisions.

in the edge plasmas with high  $q$ . The dynamics of the GAM can be characterized by the wavenumber-frequency spectrum  $E(k_r, f)$  of the GAM electric field  $E(r, t)$ , which is defined as  $E(k_r, f) = \omega / 2\pi = |\int \int E(r, t) e^{-i\omega t} e^{-ik_r r} dt dr|$ . The contour plot of  $E(k_r, f)$  of the GAM at the pedestal top without collisions is shown in Fig. 6. We can see that the GAM propagates mostly inward, which is probably due to the stronger GAM damping at the smaller radial location with a lower  $q$  value and the fact that uniform marker particle temperature is used in the simulations.

Time evolutions of volume-averaged heat conductivities for both electrons and ions are shown in Fig. 7 for the cases with or without collisions. We can see that collisions have little effects on the averaged level of the heat transport for both electrons and ions although they slightly reduce the linear growth rate. However, because of the collisional damping effects, GAM amplitudes are significantly reduced and the periodic oscillation of the heat conductivities is suppressed in the collisional cases.

## B. Peak gradient region

The current simulations with collisions conclusively demonstrate that the trapped electron mode (TEM) is the

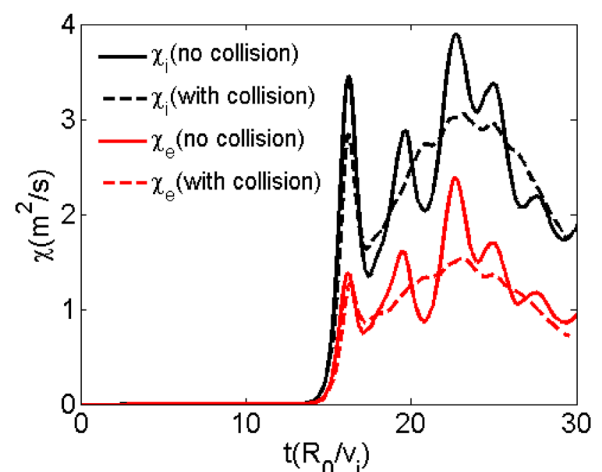


FIG. 7. Time evolutions of volume-averaged heat conductivities for both electrons and ions with or without collisions.

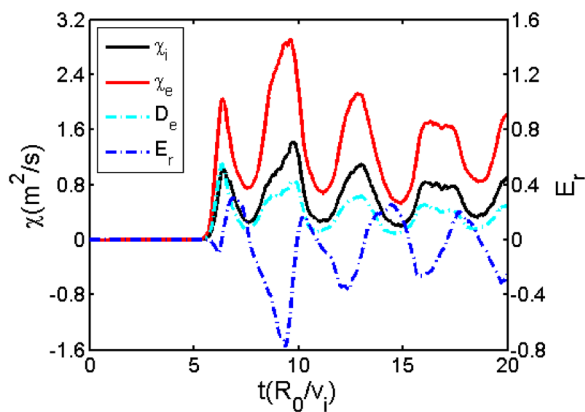


FIG. 8. Time evolutions of GAM electric field at the flux surface of  $r = 0.87a$ , volume-averaged heat conductivities for ions and electrons, and particle diffusivity for collisionless case in the peak gradient region.

most unstable electrostatic mode in the peak gradient region, consistent with our earlier collisionless simulation results reported in Ref. 12. In the current simulations with collisions, the electron is in the banana regime ( $\nu^* = 0.20$  in the peak gradient region), which significantly reduces the TEM growth rate. The TEM findings include the linear dispersion calculated from the linear stage of the nonlinear simulations and the larger electron entropy and heat fluxes (as compared to the ion counterparts) from the nonlinear simulations in Fig. 8. The TEM with a mode structure peaking at poloidal angles  $\theta = \pm\pi/2$  ( $\theta = 0$  at the outboard midplane) is the most unstable mode in the peak gradient region as observed in previous linear simulations.<sup>8</sup>

GAM is generated after nonlinear saturation. We note that GAM generation by the TEM turbulence has been previously reported by other gyrokinetic codes (e.g., Ref. 29). The GAM frequency calculated from the simulations is about  $2.49 v_i/R_0$  (approximately 30.83 kHz), which is close to  $2.39 v_i/R_0$  calculated by Equation (5). Time evolutions of volume-averaged heat conductivities for both ions and

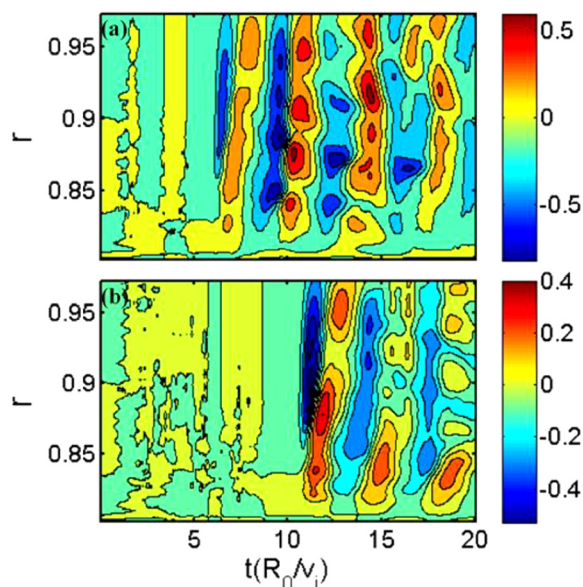


FIG. 9. GAM electric field  $E_r$  as a function of time and radial position in the peak gradient region for (a) without collisions and (b) with collisions.

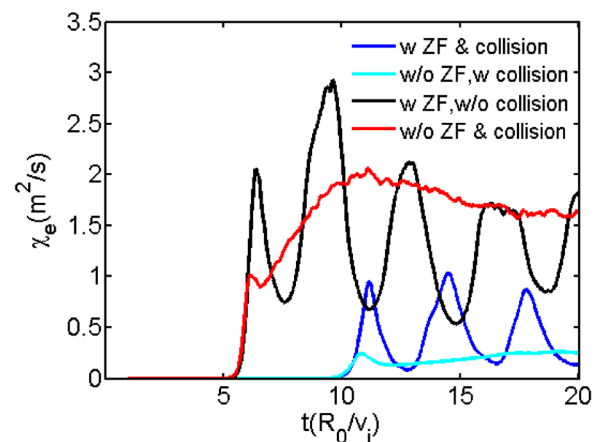


FIG. 10. Time history of volume-averaged electron heat conductivity from simulations with or without GAM or collisions.

electrons and particle diffusivity are also plotted in Fig. 8. We can see clear GAM modulation of the turbulence. The turbulence and GAM electric field exhibit an almost  $180^\circ$  phase shift, so heat conductivities and particle diffusivity oscillate at the GAM frequency.

The GAM electric field  $E_r$  is shown in Fig. 9 as a function of time and radial position. The upper panel is without collisions and the lower panel is with collisions. Again, we can see clear periodic oscillations and significant collisional damping of the GAM amplitude. Without collisions, there is no obvious propagation of GAM. Collisions significantly reduce the GAM amplitude and induce a radial propagation of GAM.

To investigate the effects of GAM and collisions on turbulence transport, four simulations with or without GAM or collisions are shown in Fig. 10. The cases without GAM are set by artificially excluding  $n = 0$  modes to illustrate the effects of these modes on turbulent transport. With collisions, the linear growth rate is significantly reduced, but the mode propagation is still in the electron diamagnetic direction. And, the electron heat transport is larger than the ion heat transport. In the nonlinear stage, we can see that electron heat conductivity saturates at a lower level for the two cases with collisions and saturates at a higher level for the two cases without collisions. We conclude that collisional effects play the dominant role in setting the level of turbulent transport because of the de-trapping processes by electron-electron and electron-ion collisions, thus effectively removing the electron drive. We can see strong GAM modulation of turbulence without collisions. However, the averaged level of the turbulent transport is less sensitive to the GAM modulation with collisions.

#### IV. CONCLUSION

Gyrokinetic simulations of electrostatic microturbulence in the edge plasmas of DIII-D shot 131997 find that the geodesic acoustic mode (GAM) is generated after nonlinear saturation both at the pedestal top and in the peak gradient region and, in turn, regulates the turbulence in both regions. Collisions significantly reduce the GAM amplitude and the associated GAM modulation of the turbulence in both

regions. Collisions have little effects on the ITG turbulent transport level in the pedestal top. On the other hand, collisional damping of the TEM significantly reduces the turbulent transport level in the peak gradient region. In the future work, the effects of sheared flows on the pedestal transport will be studied so that simulation results can be compared quantitatively to experimental measurements.

## ACKNOWLEDGMENTS

This work was supported by ITER-China Program (Grant Nos. 2013GB111000 and 2013GB112006), National Natural Science Foundation of China (Grant No. 11275162), and U.S. DOE theory Grant No. DE-SC0010416. This research used resources of the Oak Ridge Leadership Computing Facility at Oak Ridge National Laboratory (DOE Contract No. DE-AC05-00OR22725), the National Energy Research Scientific Computing Center (DOE Contract No. DE-AC02-05CH11231), and the National Supercomputing Center in Tianjin.

<sup>1</sup>W. Horton, *Rev. Mod. Phys.* **71**(3), 735 (1999).

<sup>2</sup>Z. Lin, T. S. Hahm, W. W. Lee, W. M. Tang, and R. B. White, *Science* **281**(18), 1835 (1998).

<sup>3</sup>P. W. Terry, *Rev. Mod. Phys.* **72**(1), 109 (2000).

<sup>4</sup>F. Wagner, G. Becker, K. Behringer, D. Campbell, A. Eberhagen, W. Engelhardt, G. Fussmann, O. Gehre, J. Gernhardt, G. v. Gierke, G. Haas, M. Huang, F. Karger, M. Keilhacker, O. Klüber, M. Kornherr, K. Lackner, G. Lisitano, G. G. Lister, H. M. Mayer, D. Meisel, E. R. Müller, H. Murmann, H. Niedermeyer, W. Poschenrieder, H. Rapp, H. Röhr, F. Schneider, G. Siller, E. Speth, A. Stäbler, K. H. Steuer, G. Venus, O. Vollmer, and Z. Yü, *Phys. Rev. Lett.* **49**(19), 1408 (1982).

<sup>5</sup>E. Wang, X. Xu, J. Candy, R. J. Groebner, P. B. Snyder, Y. Chen, S. E. Parker, W. Wan, G. Lu, and J. Q. Dong, *Nucl. Fusion* **52**(10), 103015 (2012).

<sup>6</sup>J. M. Canik, W. Guttenfelder, R. Maingi, T. H. Osborne, S. Kubota, Y. Ren, R. E. Bell, H. W. Kugel, B. P. LeBlanc, and V. A. Souhkanovskii, *Nucl. Fusion* **53**(11), 113016 (2013).

<sup>7</sup>F. Liu, Z. Lin, J. Q. Dong, and K. J. Zhao, *Phys. Plasmas* **17**(11), 112318 (2010).

<sup>8</sup>D. P. Fulton, Z. Lin, I. Holod, and Y. Xiao, *Phys. Plasmas* **21**(4), 042110 (2014).

<sup>9</sup>H. S. Xie and Y. Xiao, *Phys. Plasmas* **22**(9), 090703 (2015).

<sup>10</sup>W. Wan, S. E. Parker, Y. Chen, R. J. Groebner, Z. Yan, A. Y. Pankin, and S. E. Kruger, *Phys. Plasmas* **20**(5), 055902 (2013).

<sup>11</sup>D. Dickinson, S. Saarelma, R. Scannell, A. Kirk, C. M. Roach, and H. R. Wilson, *Plasma Phys. Controlled Fusion* **53**(11), 115010 (2011).

<sup>12</sup>I. Holod, D. Fulton, and Z. Lin, *Nucl. Fusion* **55**(9), 093020 (2015).

<sup>13</sup>K. Hallatschek and D. Biskamp, *Phys. Rev. Lett.* **86**(7), 1223 (2001).

<sup>14</sup>N. Winsor, J. L. Johnson, and J. M. Dawson, *Phys. Fluids* **11**(11), 2448 (1968).

<sup>15</sup>W. Zhang, Z. Lin, and L. Chen, *Phys. Rev. Lett.* **101**(9), 095001 (2008).

<sup>16</sup>Y. Xiao and Z. Lin, *Phys. Rev. Lett.* **103**(8), 085004 (2009).

<sup>17</sup>Z. Lin, W. M. Tang, and W. W. Lee, *Phys. Plasmas* **2**(8), 2975 (1995).

<sup>18</sup>T. S. Hahm, *Phys. Fluids* **31**(9), 2670 (1988).

<sup>19</sup>W. W. Lee, *J. Comput. Phys.* **72**, 243 (1987).

<sup>20</sup>A. M. Dimits and W. W. Lee, *J. Comput. Phys.* **107**(2), 309 (1993).

<sup>21</sup>S. E. Parker and W. W. Lee, *Phys. Fluids B* **5**(1), 77 (1993).

<sup>22</sup>Z. Lin, Y. Nishimura, Y. Xiao, I. Holod, W. L. Zhang, and L. Chen, *Plasma Phys. Controlled Fusion* **49**(12B), B163 (2007).

<sup>23</sup>R. J. Groebner, A. W. Leonard, P. B. Snyder, T. H. Osborne, C. F. Maggi, M. E. Fenstermacher, C. C. Petty, and L. W. Owen, *Nucl. Fusion* **49**(8), 085037 (2009).

<sup>24</sup>I. Holod and Z. Lin, *Phys. Plasmas* **14**(3), 032306 (2007).

<sup>25</sup>Z. Gao, K. Itoh, H. Sanuki, and J. Q. Dong, *Phys. Plasmas* **15**(7), 072511 (2008).

<sup>26</sup>Z. Gao, *Phys. Plasmas* **20**(3), 032501 (2013).

<sup>27</sup>X. Q. Xu, Z. Xiong, Z. Gao, W. M. Nevins, and G. R. McKee, *Phys. Rev. Lett.* **100**(21), 215001 (2008).

<sup>28</sup>H. S. Zhang and Z. Lin, *Phys. Plasmas* **17**(7), 072502 (2010).

<sup>29</sup>J. Lang, Y. Chen, and S. E. Parker, *Phys. Plasmas* **14**(8), 082315 (2007).